HHS Public Access

Author manuscript

Biosens Bioelectron. Author manuscript; available in PMC 2024 October 10.

Published in final edited form as:

Biosens Bioelectron. 2024 September 01; 259: 116321. doi:10.1016/j.bios.2024.116321.

Towards sustainable and humane dairy farming: A low-cost electrochemical sensor for on-site diagnosis of milk fever

Ali Soleimani[a], **Farbod Amirghasemi**[a], **Abdulrahman Al-Shami**[a], **Sina Khazaee Nejad**[a], **Alicia Tsung**[b], **Yuxuan Wang**[a], **Sandra Lara Galindo**[a], **Delaram Parvin**[a], **Amber Olson**[c], **Amir Avishai**[d], **Maral P.S. Mousavi**[a,*]

[a]Alfred E. Mann Department of Biomedical Engineering, Viterbi School of Engineering, University of Southern California, 1042 Downey Way, Los Angeles, 90007, California, United States

[b]Mork Family Department of Chemical Engineering and Materials Science, Viterbi School of Engineering, University of Southern California, 925 Bloom Walk HED 216, Los Angeles, 90007, California, United States

[c]Chaska Valley Veterinary Clinic, 115 W 3rd Street, Chaska, 55318, Minnesota, United States

[d]Core Center for Excellence in Nano Imaging, University of Southern California, 925 Bloom Walk, Los Angeles, 90089, California, United States

Abstract

Milk fever is a metabolic disorder that predominantly affects dairy animals during the periparturient period and within four weeks of calving. Milk fever is primarily attributed to a decrease in the animal's serum Ca^{2+} levels. Clinical milk fever occurs when Ca^{2+} concentration drops below 1.5 mM (6 mg/dL). Without prompt intervention, clinical milk fever leads to noticeable physical symptoms and health complications including coma and fatality. Subclinical milk fever is characterized by Ca^{2+} levels between 1.5 and 2.12 mM (6–8.48 mg/dL). Approximately 50% of multiparous dairy cows suffer from subclinical milk fever during the transition to lactation. The economic impact of milk fever, both direct and indirect, is substantial, posing challenges for farmers. To address this issue, we developed a low-cost electrochemical sensor that can measure bovine serum calcium levels on-site, providing an opportunity for

*Corresponding author: mousavi.maral@usc.edu (M.P.S. Mousavi).

Declaration of competing interest

The authors declare that they have no known competing financial interests or personal relationships that could have appeared to influence the work reported in this paper.

CRediT authorship contribution statement

Ali Soleimani: Writing – review & editing, Writing – original draft, Visualization, Validation, Project administration, Methodology, Investigation, Formal analysis, Conceptualization. **Farbod Amirghasemi:** Writing – review & editing, Visualization, Methodology, Investigation, Formal analysis, Conceptualization. **Abdulrahman Al-Shami:** Writing – review & editing, Methodology, Investigation, Formal analysis. **Sina Khazaee Nejad:** Writing – review & editing, Visualization, Investigation, Formal analysis. **Alicia Tsung:** Writing – review & editing, Investigation, Formal analysis. **Yuxuan Wang:** Writing – review & editing, Investigation. **Sandra Lara Galindo:** Writing – review & editing, Investigation, Conceptualization. **Delaram Parvin:** Writing – review & editing, Investigation. **Amber Olson:** Writing – review & editing. **Amir Avishai:** Investigation. **Maral P.S. Mousavi:** Writing – review & editing, Writing – original draft, Validation, Supervision, Resources, Project administration, Methodology, Investigation, Funding acquisition, Formal analysis, Conceptualization.

Appendix A. Supplementary data

Supplementary data to this article can be found online at https://doi.org/10.1016/j.bios.2024.116321.

early detection of subclinical and clinical milk fever and early intervention. This calcium sensor is a scalable solid contact ion sensing platform that incorporates a polymeric calcium-selective membrane and ionic liquid-based reference membrane into laser-induced graphene (LIG) electrodes. Our sensing platform demonstrates a sensitivity close to the theoretical Nernstian value (29.6 mV/dec) with a limit of detection of 15.6 μM and selectivity against the species in bovine serum. Moreover, our sensor can detect Ca^{2+} in bovine serum with 91% recovery.

Keywords

Milk fever; Potentiometric sensing; Laser induced graphene (LIG); Calcium sensing; Frugal sensors; Point-of-care on-site analysis

1. Introduction

Milk fever, or parturient paresis, is a metabolic disorder that occurs in dairy animals. The risk of the disease increases by onset of periparturient and within days of calving Oetzel. Factors such as age and diet influence the incidence of milk fever Payne (1977). The primary cause and indicator of milk fever is a significant decrease in blood calcium levels (known as hypocalcemia) Lean et al. (2006); Boda et al. (1954). Normal calcium levels in bovine serum range from 2.12 mM to 2.5 mM (8.48–10 mg/dL), and serum calcium levels lower than 2.12 mM (8.48 mg/dL) indicate milk fever. The stages of milk fever are categorized as subclinical and clinical milk fever Lean et al. (2006). Clinical milk fever happens when the calcium level in the serum drops below 1.5 mM (6 mg/dL), which is accompanied by symptoms such as loss of appetite, tetany, urinary retention, and lateral recumbency. If left untreated, clinical milk fever can quickly result in animal fatality. Subclinical milk fever occurs when serum calcium levels range between 1.5 mM and 2.12 mM (6–8.48 mg/dL). Unlike clinical milk fever, subclinical milk fever does not have any physical symptoms Thilsing-Hansen et al. (2002). The reported incidence rates of milk fever in prior studies exhibit significant variability among different herds. Some herds demonstrate rates below 1%, whereas others exhibit incidences exceeding 25% Mullen (1975). A meta-analysis study on 135 controlled trials by Lean et al. also confirm the variability in the incident rate of milk fever, reporting a range of 0–83% with a mean value of 21% Lean et al. (2006). A study by Reinhardt et al. revealed that subclinical hypocalcemia is prevalent in 50% of multiparous dairy cows as they transition to lactation Reinhardt et al. (2011). Roche and Berry showed that the risk of milk fever increases by 9% after each successive lactation Roche and Berry (2006).

Direct economic losses associated with milk fever result from reduced milk production, animal mortality, and treatment costs. Furthermore, indirect economic impacts include increased risks of related health problems, calving complications, decreased productive life and fertility Bzuneh et al. (2020). Since a systematic estimate of economic burden of milk fever in the US was not found, we estimated the costs associated with milk fever in the United States. Based on United States Department of Agriculture (USDA), there are 9.4 million milking cows in the US; the cost for treatment of the milk fever is $150 USD per cow. Considering the average milk fever incidence rate of 21% reported by Lean et al., the treatment cost of the milk fever in US is $296 million USD. However, the real

number should be much higher since the prevalence of milk fever increases by number of parturitions and age. Moreover, indirect economic losses that have arisen from reduced milk production, as well as decreased productive life and fertility, have not been considered in this estimation Matlock (2023); Reinhardt et al. (2011). Milk fever puts a large burden on agriculture-focused regions globally, a study by Cariappa estimated the economical loss of milk fever in Heryana, India to be $137 million USD Cariappa et al. (2021).

The asymptomatic nature and elevated prevalence of subclinical milk fever contribute to a significant increase in the hidden economic burdens compared to clinical milk fever Oetzel (2012). The costs related to subclinical milk fever are estimated to be fourfold higher than those associated with clinical milk fever due to the higher incidence rate of subclinical milk fever Oetzel (2012). Moreover, subclinical cows has longer median open (non-pregnant) days compared with healthy cows (124 vs. 109 days) Melie. The longer interval between calving and conception impacts the overall reproductive efficiency of the herd. Consequently, timely diagnosis of subclinical milk fever emerges as a pivotal strategy for mitigating both financial losses and welfare impacts on dairy animals. Early detection and intervention not only reduce economic burdens, but also prevent and alleviate discomfort experienced by animals. The pain that animals experience is much higher at the clinical milk fever stage, underscoring the importance of implementing preventive measures and diagnostic strategies to effectively manage subclinical cases in dairy herds.

Currently, milk fever is diagnosed using history taking, laboratory techniques, and clinical examination. History taking involves gathering information about the cow's age, breed, stage of lactation, milk yield and calving day Bzuneh et al. (2020). The most accurate and reliable method for milk fever diagnosis is laboratory testing to determine if the blood calcium level falls within the range associated with milk fever. Since severe hypocalcemia requires prompt treatment, there would not be enough time for laboratory verification. Therefore, implementing a point-of-care (PoC) system can enable timely diagnosis of milk fever in the field. Moreover a PoC system for the regular screening of serum Ca^{2+} concentrations in dairy animals can facilitate the early detection of subclinical milk fever. Early detection can prevent onset of clinical milk fever through early intervention. However, despite the benefits of PoC technologies for frequent screening of milk fever, there are currently no tools that can meet this need in an affordable manner.

In this work, we developed a rapid, low-cost, and portable device to assess Ca^{2+} concentrations in the field in individual cows. This invention allows farmers to implement more effective strategies for monitoring and preventing milk fever to decrease both the direct and indirect costs associated with hypocalcemia. We employ a scalable fabrication technique based on laser engraving of polyimide films. The advantage of LIG over other materials is the scalability and cost-effectiveness of its fabrication that makes it suitable for on-site sensors. Moreover, the 3D porous structure of LIGs interfacing the membrane creates a high capacitance that increases the stability of potentiometric sensors. Since its discovery in 2004 Novoselov et al. (2004), graphene has attracted growing interest for its applications in biosensing due to its flexibility, mechanical strength, electrical conductivity, thermal conductivity, and electron mobility Morales-Narváez et al. (2017); Jiang et al. (2020); Flauzino et al. (2022); Goldoni et al. (2021); Zhang et al. (2022). However, high temperature

and multi-step synthesis of graphene, which are expensive and time-consuming, limited their application, especially for PoC testing Abbas et al. (2022). To overcome this issue, in 2014, Lin et al. utilized CO_2 laser pulses to convert sp3 carbons of commercials polymers to sp2 carbon using a one-step photo-thermal reaction, reducing the cost and complication of the graphene synthesis, thus broadening its applications Lin et al. (2014). Though this technique can apply toward various materials, polyimide remains the most popular option for LIG synthesis due to its affordability, accessibility, and flexibility Wan et al. (2020). Recently, LIG-based sensors have been developed for detection of various biomarkers Soares et al. (2023); Hjort et al. (2022); Kucherenko et al. (2021); Soupir et al. (2022); Barber et al. (2021); Al-Shami, 2024; Kucherenko et al. (2020); Teekayupak et al. (2023); Wan et al. (2020); Lee et al. (2022); Amirghasemi et al. (2023); Khazaee Nejad et al. (2024). To the best of our knowledge, this work presents the first LIG-based sensor for detection of calcium in bovine serum, and in general, the first PoC test for rapid on-site diagnosis of milk fever based on serum Ca^{2+} level.

2. Materials and methods

2.1. Material and apparatus

Electrical-Grade Kapton® Polyimide Film (12 inches in length × 12 inches in width × 0.005 inches in thickness) and Electrical-Grade, Adhesive Back Kapton® Polyimide Film (12 inches in length × 12 inches in width × 0.002 inches in thickness) were purchased from McMaster-Carr, USA. Extremely conductive elastomeric silver ink (127–07) was purchased from Creative Materials, USA. Potassium tetrakis(4-chlorophenyl)borate (KTCPB), calcium ionophore IV, 2-nitrophenyl octyl ether (o-NPOE), high molecular-weight poly(vinyl chloride) (PVC), tetrahydrofuran (THF), sodium chloride, D-(+)-Glucose, urea, creatinine, lactate, and bovine serum albumin (BSA) were obtained from Sigma Aldrich, USA. Potassium chloride and magnesium chloride were obtained from Macron. Calcium chloride was purchased from Beantown Chemical. 1-octyl-3-methylimidazolium bis(trifluoromethylsulfonyl) imide (MeOctIm TFSI) was acquired from Alfa Aeser. Bovine serum samples were obtained from three different vendors including Thermo Fisher Scientific, Sigma Aldrich, and VWR. All aqueous solutions were prepared using deionized water (resistivity of 18.2 MΩ·cm) obtained from Millipore Milli-Q water purification system.

Epilog Mini 24 Laser engraver was utilized for the fabrication of laser-induced graphite on polyimide films. All potentiometric measurements were conducted using an EMF 16-channel potentiometer (Lawson Labs in Malvern, PA). Electrochemical impedance spectroscopy (EIS), Chronopotentiometry and cyclic voltammetry measurements were performed using the CHI 760E electrochemical analyzer (CH Instruments, TX, USA). Scanning electron microscopy (SEM) analysis was conducted using a Nova NanoSEM 450 field emission SEM (FEI, OR, USA), using 3 keV electron beam energy and 3.5 spot size. Energy dispersive X-ray (EDX) characterization was conducted using the Oxford UltimMax 170 Silicon Drift Detector (Oxford instrument, UK). X-ray photoelectron spectroscopy (XPS) characterization was conducted using Kratos Axis Ultra DLD (Kratos Analytical, UK). Raman spectroscopy characterization was conducted using the Horiba XploRA Raman

Microscope System (Horiba, Japan). Horiba LAQUAtwin Ca-11 Compact Calcium Pocket Tester (Horiba, Japan) was utilized as a commercially available sensor to perform a comparative analysis between the outcomes obtained from the fabricated sensor and the commercial sensors. Sensit BT (PalmSens BV, Utrecht, Netherlands) was used to conduct wireless measurements. ThermoFisher, Talos 200C (200 kV), in transmission electron microscopy (TEM) mode, and Velox software were used for TEM analysis. In order to perform TEM, the LIGs were peeled off from a PI film and sonicated in chloroform before being transferred to Carbon Type-B Copper TEM grid. We removed the Formvar layer by dipping the grids into chloroform before transferring the samples on it.

2.2. LIG fabrication

We first rinsed the PI films with acetone, isopropyl alcohol (IPA), and deionized water. Then, we put the films in oven at 100 °C for 5 min to dry. In the next step, we started the engraving process of LIGs using a CO_2 laser with 5% power, 10% speed, and 1200 DPI on autofocus mode. After the laser engraving process finished, we applied silver ink on the electrodes' contact pad in order to have a better electrical connection. In the last step, we insulated our electrodes using Kapton tape.

2.3. Preparation of calcium and reference membrane and electrodes

We prepared our Ca^{2+} selective membrane by mixing 330 mg of PVC, 660 mg of o-NPOE, 2 mg of KTCPM, and 10 mg Ca^{2+} ionophore IV in 3 ml THF. In order to prevent the overnight conditioning of the membrane in Ca^{2+} containing solution to exchange K^{+} with Ca^{2+}, we spiked our membrane solution with 5.4 μL of 1 M $CaCl_2$ solution and mixed them overnight. We drop-casted two droplets of 20 μL of membrane solution on the electrode and allowed the solvent to evaporate overnight. To prepare the reference membrane, we mixed 100 mg of MeOctIm TFSI with 300 mg of PVC and 600 mg of o-NPOE in 3.0 mL of THF, and stirred the solution overnight. Finally, we drop-casted two droplets of 20 μL of membrane solution on the electrode and left overnight to dry.

3. Results and discussion

3.1. Design and operation of the sensing platform

Fig. 1 shows the design and operation of our Ca^{2+} sensing platform. The sensor consist of two electrodes: a calcium-selective electrode, and an ionic liquid (IL)-based reference electrode. The sensing platform is connected to a portable wireless potentiostat that performs the electrochemical analysis and transmits the data to a smart phone. In order to avoid any error in the measured concentrations due to the calibration shift during the shelf storage and sensor-to-sensor variability, a two-point calibration should be performed before measuring the Ca^{2+} in serum sample. The calibration starts by immersing the sensing platform in the first calibration solution and waiting for 1 min for signal readout. Then, the sensing platform should be dried with a tissue paper and immersed in the second calibration solution. Next, the sensor is exposed to the serum for 1 min for the final measurement.

The LIG-based Ca^{2+} sensor is fabricated using a scalable and inexpensive method that makes them a perfect choice for in-field, frequent monitoring of calcium. Moreover, the

LIG sensors are flexible, and due to their highly porous structure, they exhibit stable and reliable signal. Our sensing platform work based on potentiometric recognition. Potentiometric sensing allows rapid, sensitive, and selective detection of ions in complex matrices Bakker et al. (1997); Bühlmann et al. (2012); Bakker (1997). The basic working principle of potentiometric sensors is the sample's activity-dependant electromotive force (emf) generated at the interface of the sample and an ion-selective membrane (ISM) Bakker et al. (1997). The ISM is in contact with an ion-to-electron transducer Lyu et al. (2020). The ion-to-electron transducer maintains a stable emf at its interface with ISM through redox capacitance or electric double-layer (EDL) capacitance Hu et al. (2016); Veder et al. (2013); Cuartero et al. (2016). Several materials have been used as ion-to-electron transducer interfaces to produce stable and reproducible signal including conductive polymers Cadogan et al. (1992); Bobacka (2006), nanomaterials Zou et al. (2013, 2014), and carbon-based materials Lai et al. (2007); Li et al. (2012); Liu et al. (2020). In this work, we used LIG as ion-to-electron transducer to utilize its high conductivity, porosity, and low cost of fabrication.

3.2. LIG characterization

The fabrication process of laser-induced graphene (LIG) involves a photothermal reaction designed to convert sp3 carbons to sp2. The initiation of this process requires an amount of energy provided by a laser source, making the precise control of laser energy crucial for obtaining an optimal LIG layer. To optimize the laser energy input on the polyimide (PI) film, we performed a comparative study. We varied the power and speed of the laser machine within the ranges of 3%–10% and 5%–15% of the maximum speed and power respectively (where the maximum speed is 82 inch/s, and the maximum power is 30 W). Our results indicate that using a 5% speed and 10% power setting yields the lowest conductivity, with neither mechanical delamination of the graphene layer nor carbon powder formation (Fig. S1). This comparative analysis aids in identifying the optimal conditions for achieving a desired LIG layer with specific electrical and structural properties. We used the scanning electron microscopy (SEM) technique to characterize the produced laser-induced graphitic surface. As illustrated in Fig. 2(A and B), the laser ablation of polyimide (PI) film led to the creation of a three-dimensional porous carbon structure characterized by extended fibers. Examination of the cross-section SEM image of the calcium-selective membrane on the LIG structure (Fig. 2(C)) revealed the homogeneous integration of the membrane within the LIG fibrous surface. Furthermore, no entrapped bubbles in the membrane were observed, which provides the sensor with better mechanical stability and stable performance.

We employed energy dispersive X-ray Spectroscopy (EDX) to investigate the elemental composition of the generated graphitic carbon. The EDX analysis, (Fig. 2(D)), shows that the surface of the LIG structure is mostly composed of carbon with negligible traces of oxygen and nitrogen. This indicates the effective carbonization of the polyimide film through the laser engraving process.

Raman spectroscopy was used for studying the structural characteristics of the produced LIG. Raman spectrum in (Fig. 2 (E)) shows the three main characteristic peaks of 3D graphitic structure. The G peak that appears around 1533 cm^{-1} indicates the vibration mode

of the sp2 carbon atoms in the graphene lattice, whereas the D peak around 1350 cm^{-1} denotes the presence of structural disorders and defects in the LIG graphene lattice. The 2D peak at ≈ 2690 cm^{-1} indicates the multilayered graphene structure. From the Raman spectrum, the I_{2D}/I_G ratio (≈0.32) indicates the formation of > *five* graphene layers Bleu et al. (2019). The XPS survey spectrum in Fig. 2 (F) reveals the presence of oxygen and carbon content in the produced LIG samples. The C 1s peak at approximately 284.5 (Fig. 2 (F)) results from the convolution of four peaks at 284.2, 284.7, 285.8, and 288.6 eV, corresponding to C=C, C–C, C–O, and C=O bonds respectively. Furthermore, the high-resolution O 1s spectrum shown in (Fig. 2 (G)) reveals the presence of C–O, C=O, and O=C–O–H chemical bonds at 531.6, 532.9, and 535.1 eV, respectively Ren et al. (2018). Here, we observed a difference in the oxygen composition of LIG when employing X-ray photoelectron spectroscopy (XPS) and energy-dispersive X-ray spectroscopy (EDX) techniques. This variation suggests the localization of oxygen bonds on the surface, as the XPS technique measures within the top few nanometers of samples, whereas EDX goes deeper until 2–5μm Titus et al. (2019); Hues and Lovejoy (2018); Mather (2009); Omidi et al. (2017).

We assessed the electrochemical performance of the LIG-based electrodes (diameter of working electrode = 3 mm) using cyclic voltammetry in 2.0 mM $[Fe(CN)_6]^{3-/4-}$ and 0.1 M KCl. The cyclic voltammograms were recorded at a scan rate from 20 to 100 mVs^{-1} (Fig. 2 (I)). The oxidation and reduction current values and the peak separation increase with increasing scan rate indicating the electrochemical active LIG surface with controlled diffusion reaction.

We performed TEM characterization to gain a comprehensive insight into the LIGs. In Fig. 2(J)–a low magnification TEM image of the LIG flakes is presented. Further, higher resolution TEM images depicted in Fig. 2 (K–L) reveal the formation of ripple-like structures on the LIGs. Particularly, Fig. 2 (L) highlights a lattice distance of approximately 3.4 Å, corresponding to the lattice space between (002) planes in graphitic materials Lin et al. (2014).

3.3. Sensing mechanism and characterization of calcium sensor

The sensing mechanism in the potentiometric sensors relies on the charge separation at the sample-membrane interface. This charge separation generates an emf that relates to the activity of ion of interest in the sample based on the Nernst equation Bühlmann et al. (2012); Bakker and Pretsch (2002); Bakker (1997); Hu et al. (2016):

$$E = E^{\circ} + \left(\frac{59.2mV}{z_i}\right) log(a_i + k_{i,j}^{Pot} a_j^{z_i/z_j}) \quad (1)$$

where,

$$a_i = \gamma_i C_i \quad (2)$$

where $E^0(\mathrm{mV})$ is the standard potential, R is universal gas constant, T is temperature, Z_i is the charge of the ion of interest, F is Faraday's constant, a_i shows the activity of ion of interest, a_j is the activity of interfering ion, $k_{i,j}^{pot}$ is the selectivity coefficient of the sensor for ion of interest over the interfering ion, and γ_i is the activity coefficient. As shown in the equation (1) and (10) fold change in the activity results in $\frac{59.2mV}{z_i}$.

We validated the sensitivity of our sensor toward Ca^{2+} against a free-flow double-junction external reference electrode Fig. 3(A–B). For this purpose, we recorded the emf values of the sensor by successively diluting the aqueous solution, allowing it to equilibrate for 1 min, and averaging the last 10 s data. Fig. 3(A) shows the calibration curve of our sensor indicating sensitivity of 27.7 ± 0.46 mV/dec (n = 5) that is close to the theoretical Nernstian slope ($29.6\frac{mV}{dec}$). Moreover, the limit of detection (LOD) of our sensor is 15.16 μM which is two orders of magnitude lower than the therapeutic range.

To confirm the selectivity of the sensor, we examined the performance of our sensors in an artificial bovine serum (a-serum). The sensitivity and limit of the detection of the sensor in a-serum are 26.98 ± 0.13 and 17.96 μM respectively. These results indicate a sensitivity close to the theoretically expected value and an LOD that is two orders of magnitude lower than the physiological relevant range, which confirms the sensor's selectivity and sensitivity for detection of Ca^{2+} in serum.

To further validate the selectivity of our sensor, we initially determined the electromotive force (emf) of the sensor in the presence of 1 mM Ca^{2+}. Subsequently, we conducted emf measurements when co-presencing 1 mM Ca^{2+} with other serum-interfering ions and biological constituents at their physiologically relevant concentrations (Fig. 3 (G)). All emf readouts exhibited remarkable similarity, confirming the sensor's selective response to Ca^{2+}. Furthermore, the observed reduction in emf, in response to the Ca^{2+} and urea mixture, is attributed to the tendency of calcium salts to form complexes with urea as reported in literature Pande and Bhatnagar (1958).

Reversibility is another important feature of sensors ensuring the ability of the sensor to revert to its original baseline after repeated exposure cycles. To confirm the reversibility of our fabricated sensor, we first exposed our sensor to a solution containing 10 mM Ca^{2+} and recorded the emf response of our sensor. Then, we exposed the sensors to solutions containing physiologically relevant concentrations of ions and biologicals before recording the emf. After each exposure to the interfering ions and biologicals, we recorded the emf in the solution containing 10 mM Ca^{2+}. Fig. 3(H) shows that the sensor's emf readout returned to a similar baseline readout, indicating the remarkable reversibility of the sensor.

Signal stability is a crucial factor in solid-contact ion-selective electrodes (SC-ISEs). Having a high capacitance at the interface of the ion-to-electron transducer and ISM increases the emf stability at this interface, yielding a stable sensor response. The 3D porous structure of LIGs (Fig. 2 (A–C)) makes them an excellent choice for ion-to- electron transducer material due to their high surface area. To validate the stability of the sensor, we performed a chronopotentiometry experiment to measure the capacitance at this interface and compared

it with the capacitance at the interface of coated Pt wire electrode. In this experiment, we subjected the system to a perturbation current of ±1 nA and observed the corresponding changes in potential over a specified time period before calculating the capacitance based on Equation (3).

$$i = C\frac{dV}{dt} \tag{3}$$

where i is electrical current, C is capacitance, and $\frac{dV}{dt}$ is the discharge.

After obtaining a discharge of 2.2 mV over a ±1 nA perturbation current, we calculated a double-layer capacitance of 27.3 μF for the interface between the ISM and LIG. A comparative measurement with a Pt-coated Ca^{2+} sensor shows that the LIG Ca^{2+} sensor exhibited higher stability and double-layer capacitance. The 27.3 μF is comparable to other reported capacitance values for ion-to-electron transducer materials, but is not among the highest capacitance values. Since this sensor is intended for short term on-site measurements, the sensor performance and signal stability meet the demand while allowing for a low-cost fabrication process.

A discharge equivalent to 2.2 mV was observed over the course of 60 s, leading to a capacitance of 27.3 μF at membrane-Pt interface. The fourfold increase in the capacitance confirms the high signal stability in LIG-based ion selective electrodes. We determined the resistivity of the Ca^{2+}-selective membrane through the application of electrochemical impedance spectroscopy (EIS). Fitting the data to an equivalent Randles circuit resulted in a membrane resistivity of 0.7 $M\Omega$ Ong et al. (2023); Lazanas and Prodromidis (2023).

3.4. Reference mechanism and characterization of reference electrode

Thus far, all the emf data of the Ca^{2+} sensor were measured with respect to a free-flow double junction external reference electrode. This reference electrode presents drawbacks such as bulkiness, fragility, susceptibility to liquid junction clogging, and the potential for sample contamination. Additionally, its challenging miniaturization further hinders integration into point-of-care applications Guth et al. (2009); Lingenfelter et al. (2019); Inzelt et al. (2013). To address these limitations, various strategies have been explored. Utilization of a polyvinyl borate (PVB)-based membrane as a miniaturized reference electrode was proposed by Guinovart et al.Guinovart et al. (2014) While PVB-based reference membranes are widely employed in PoC applications, they necessitate prolonged conditioning, and their sensitivity to chloride concentration remains a concern. To avoid these limitations, we utilized an ionic liquid (IL)-based polymeric membrane as our reference electrode. The referencing mechanism of the IL-based reference electrode is based on the continuous partitioning of cations and anions between the aqueous and water-immiscible phases Kakiuchi (2008); Kakiuchi et al. (2007). We validated the performance of our electrodes by monitoring the reference potential compared to an external free-flow reference electrode in solutions of common interfering ions present in blood serum (concentration changed via successive dilution, Fig. 4A–D). The IL-based reference

electrodes showed a sample-independent signal in the range of 10^{-2} to 10^{-6} M of Ca^{2+}, K^{+}, and Mg^{2+}, as well as a stable signal in the range of 10^{-1} to 10^{-6} of Na^{+}. These concentration ranges cover the physiological ranges of these ions in serum and go orders of magnitude beyond the physiological ranges as well. The measured slopes of reference potential vs. logarithm of concentration of ions were 0.15 ± 0.44 (for Ca^{2+}), 0.8 ± 0.66 (for Na^{+}), 0.46 ± 0.12 (for K^{+}), and 0.8 ± 0.16 mV/dec (Mg^{2+}). The slopes close to zero demonstrate that the reference potential does not depend on concentration of different ionic compounds in the sample. To confirm the stability and independence of reference potential in a more complex solution, we evaluated the performance of the IL-based reference electrode by diluting the Ca^{2+} concentration in the artificial serum. The reference electrode shows a stable signal with 0.56 ± 0.54 mV/dec change in the range of 10^{-2} to 10^{-6} M Ca^{2+} (Fig. 5(E–F)).

We evaluated the performance of the reference electrode in bovine serum. Fig. 4(G) shows the stable signal of the reference electrode in different concentration of Ca^{2+} in bovine serum. Our results indicate −1.38 ± 0.27 mV change in the emf of the senor, which shows the ability of our reference electrode to provide a stable reference potential for measurements.

After a thorough evaluation of the reference and ion-selective electrodes, we evaluated the performance of the full electrochemical cell (LIG-based Ca^{2+} sensor and LIG-based reference electrode). After serial dilutions of Ca^{2+} in both deionized water and a-serum, our sensing platform exhibited sensitivities of 25.42 ± 0.92 mV/dec and 24.4 ± 1.1 mV/dec respectively (Fig. 4(H and I)). We achieved a slope close to the theoretically expected Nernstian value, with an LOD of 3.1 μM in deionized water and 3.4 μM in a-serum, which are both lower than the physiologically relevant range.

3.5. Sensor performance in bovine serum

Fig. 5(A) shows the performance of the calcium sensor in response to successive spikes of bovine serum with $CaCl_2$. The sensor responded quickly to increased Ca^{2+} concentrations in bovine serum, confirming its sensitivity and selectivity. The sensors showed a sensitivity of 20.61 ± 0.14 mV in the clinically relevant range of calcium in the serum. To insure the accuracy of our sensors in measurement of calcium in bovine serum, we measured the serum Ca^{2+} concentration and compared the result with a commercially available Ca^{2+} sensor. We performed the two-point calibration to correct for the sensor-to-sensor E_0 reproducibility and shift in slope for E_0 of the sensor during the storage. The calibration procedure was initiated by immersing the sensors in aqueous solutions of artificial serum containing $CaCl_2$ at concentrations of 0.5 mM and 5 mM ((Fig. 5(C)). Subsequently, the sensors were introduced into serum solutions, and the calcium concentration within the serum was determined. Table 1 shows the calculated calcium concentrations in serum, indicating a deviation of 4.8% from the values obtained through commercial sensor measurements.

In order to show the capability of our sensing platform, we replaced the commercial double junction free-flow reference electrode with the IL-based reference. Our findings revealed a notable discrepancy when compared to the measurements obtained from the commercially available sensor. Subsequently, we conducted an investigation into the signal alteration of our reference electrode during the transition from the calibration solution to the serum. Fig.

5(D) demonstrated a shift of 6.39 ± 0.22 mV in reference potential upon changing from the aqueous artificial serum solution (calibration solution) to the serum. This signal shift was attributed to variations in the hydrophobicity between the aqueous artificial serum and serum matrices. The reference potential is determined based on the partition coefficient of the ionic liquid between the reference membrane and sample. There are major differences between a simple a-serum containing only inorganic content of serum and the complex serum environment. Therefore, the partition coefficient of ionic liquid will change between the calibration solution and serum matrix, causing a shift in reference potential. To further investigate the shift in potential, three distinct batches of electrodes were assessed in three different bovine serum samples from different sources. We immersed the reference electrode in different Ca^{2+} concentration in a-serum and then in bovine serum, and recorded the signal change after transition from a-serum to bovine serum (Fig. 5(E)). A signal shift of 6.63 ± 0.57 mV across different serum samples compared to a-serum was observed. We performed a correction to the recovery response of our sensing platform by adjusting the shift in reference electrodes potential. Fig. 5(F) shows the recovery plot of our sensing platform. The results prior to reference error correction shows an error of 34.36 % (red point). After correcting for the reference shift, the calculated error for the sensing platform was 9.32%, which is an acceptable margin for the diagnosis of milk fever on-site and continuous monitoring of Ca^{2+} in bovine serum.

4. Conclusion

Milk fever is a metabolic disorder that affects diary animals mostly during periparturient and the period of four weeks before and after calving. The primary cause of the milk fever is a decline in the animal's Ca^{2+} level. Milk fever has direct and indirect economical impact on farmers, in addition to the pain and discomfort experienced by the animal. However, despite the prevalence and economic impact of milk fever, there are currently no low-cost PoC Ca^{2+} sensors available for milk fever diagnosis.

In this work, we developed a low-cost, rapid LIG-based PoC potentiometric sensor for on-site diagnosis of subclinical and clinical milk fever. Our LIG-based sensing platform incorporates both solid-contact ISE and reference electrodes into a complete PoC sensing package. To the best of our knowledge, this is the first PoC sensor for diagnosis of bovine milk fever. We fabricated our Ca^{2+} sensor using laser engraving, which is cost-effective, scalable, and rapid. Moreover, the 3D-porous LIG acts as an ion-to-electron transducer with high surface area and high capacitance to ensure a stable emf of the sensor. Our sensor shows remarkable sensitivity, selectivity, and reversibility and accuracy. We compared the results of our sensor with a commercially available Ca^{2+} sensor. We achieved 6.25%–9.32% error in the measurements, which is acceptable for on field diagnosis of milk fever using a low-cost sensor.

Future research will focus on fabrication of a calibration-free sensor for the detection of Ca^{2+} ions, aiming to streamline the sensor's application. Additionally, there will be an emphasis on developing both software and hardware capable of recording and archiving sensor readouts, thereby enhancing the dataset quality for history-taking analysis on the farm.

Supplementary Material

Refer to Web version on PubMed Central for supplementary material.

Acknowledgements

Maral P.S. Mousavi acknowledges the NIH Director's New Innovator Award (DP2GM150018), USC Women in Science and Engineering (WiSE) seed funding, USC Zumberge Diversity and Inclusion Award, and 3M nontenured faculty award. Abdulrahman Al-Shami, Farbod Amirghasemi, Ali Soleimani, S. Khazaee Nejad, Sandra lara Galindo, and Delaram Parvin thank the University of Southern California Viterbi Graduate Fellowship. All authors thank the Core Center of Excellence in Nano Imaging at the University of Southern California for their suggestions in SEM, XPS, and TEM characterization.

Data availability

Data will be made available on request.

References

Abbas Q, Shinde PA, Abdelkareem MA, Alami AH, Mirzaeian M, Yadav A, Olabi AG, 2022. Graphene synthesis techniques and environmental applications. Materials 15, 7804. [PubMed: 36363396]

Amirghasemi F, Al-Shami A, Ushijima K, Mousavi MP, 2023. Selective and Biocompatible Detection of Acetylcholine with a Fluorous Potentiometric Laser-Induced Graphene Sensor.

Al-Shami Abdulrahman, et al. , 2024. SPOOC (Sensor for Periodic Observation of Choline): An Integrated Lab-on-a-Spoon Platform for At-Home Quantification of Choline in Infant Formula. Small 2311745.

Bakker E, 1997. Selectivity of liquid membrane ion-selective electrodes. Electroanalysis 9, 7–12.

Bakker E, Bühlmann P, Pretsch E, 1997. Carrier-based ion-selective electrodes and bulk optodes. 1. general characteristics. Chem. Rev. 97, 3083–3132. [PubMed: 11851486]

Bakker E, Pretsch E, 2002. Peer reviewed: the new wave of ion-selective electrodes. Anal. Chem. 74, 420–A. [PubMed: 11811417]

Barber R, Cameron S, Devine A, McCombe A, Pourshahidi LK, Cundell J, Roy S, Mathur A, Casimero C, Papakonstantinou P, et al. , 2021. Laser induced graphene sensors for assessing ph: application to wound management. Electrochem. Commun. 123, 106914.

Bleu Y, Bourquard F, Loir AS, Barnier V, Garrelie F, Donnet C, 2019. Raman study of the substrate influence on graphene synthesis using a solid carbon source via rapid thermal annealing. J. Raman Spectrosc. 50, 1630–1641.

Bobacka J, 2006. Conducting polymer-based solid-state ion-selective electrodes. Electroanalysis. Int. J. Devoted Fundament. Practic. Aspect. Electroanalys. 18, 7–18.

Boda J, Cole H, et al. , 1954. The influence of dietary calcium and phosphorus on the incidence of milk fever in dairy cattle. J. Dairy Sci. 37, 360–372.

Bühlmann P, Chen L, Steed J, Gale P, 2012. Supramolecular Chemistry: from Molecules to Nanomaterials.

Bzuneh E, Alemneh T, Getabalew M, 2020. Milk Fever (Parturient Paresis) and its Economic Impact in Dairy Cattle Production.

Cadogan A, Gao Z, Lewenstam A, Ivaska A, Diamond D, 1992. All-solid-state sodium-selective electrode based on a calixarene ionophore in a poly (vinyl chloride) membrane with a polypyrrole solid contact. Anal. Chem. 64, 2496–2501.

Cariappa A, Chandel B, Sankhala G, Mani V, Sendhil R, Dixit A, Meena B, 2021. Estimation of Economic Losses Due to Milk Fever and Efficiency Gains if Prevented: Evidence from haryana, india arXiv preprint arXiv:2105.09782.

Flauzino JM, Nguyen EP, Yang Q, Rosati G, Panáček D, Brito-Madurro AG, Madurro JM, Bakandritsos A, Otyepka M, Merkoçi A, 2022. Label-free and reagentless electrochemical

genosensor based on graphene acid for meat adulteration detection. Biosens. Bioelectron. 195, 113628. [PubMed: 34543917]

Goldoni R, Farronato M, Connelly ST, Tartaglia GM, Yeo WH, 2021. Recent advances in graphene-based nanobiosensors for salivary biomarker detection. Biosens. Bioelectron. 171, 112723. [PubMed: 33096432]

Guinovart T, Crespo GA, Rius FX, Andrade FJ, 2014. A reference electrode based on polyvinyl butyral (pvb) polymer for decentralized chemical measurements. Anal. Chim. Acta 821, 72–80. [PubMed: 24703216]

Guth U, Gerlach F, Decker M, Oelßner W, Vonau W, 2009. Solid-state reference electrodes for potentiometric sensors. J. Solid State Electrochem. 13, 27–39.

Hjort RG, Soares RR, Li J, Jing D, Hartfiel L, Chen B, Van Belle B, Soupir M, Smith E, McLamore E, et al. , 2022. Hydrophobic laser-induced graphene potentiometric ion-selective electrodes for nitrate sensing. Microchim. Acta 189, 122.

Hu J, Stein A, Bühlmann P, 2016. Rational design of all-solid-state ion-selective electrodes and reference electrodes. TrAC, Trends Anal. Chem. 76, 102–114.

Hues SM, Lovejoy L, 2018. Ultratrace impurity analysis of wafer surfaces. In: Handbook of Silicon Wafer Cleaning Technology. Elsevier, pp. 701–741.

Inzelt G, Lewenstam A, Scholz F, 2013. Handbook of Reference Electrodes, vol. 541. Springer.

Jiang Z, Feng B, Xu J, Qing T, Zhang P, Qing Z, 2020. Graphene biosensors for bacterial and viral pathogens. Biosens. Bioelectron. 166, 112471. [PubMed: 32777726]

Kakiuchi T, 2008. Mutual solubility of hydrophobic ionic liquids and water in liquid-liquid two-phase systems for analytical chemistry. Anal. Sci. 24, 1221–1230. [PubMed: 18845878]

Kakiuchi T, Yoshimatsu T, Nishi N, 2007. New class of ag/agcl electrodes based on hydrophobic ionic liquid saturated with agcl. Anal. Chem. 79, 7187–7191. [PubMed: 17708675]

Khazaee Nejad S, Ma H, Al-shami A, Soleimani A, Mohamed MA, Dankwah P, Lee HJ, Mousavi M, 2024. Sustainable agriculture with leafs: a low-cost electrochemical analyzer of foliage stress. Sens. Diagn. 10.1039/D3SD00296A.

Kucherenko IS, Chen B, Johnson Z, Wilkins A, Sanborn D, Figueroa-Felix N, Mendivelso-Perez D, Smith EA, Gomes C, Claussen JC, 2021. Laser-induced graphene electrodes for electrochemical ion sensing, pesticide monitoring, and water splitting. Anal. Bioanal. Chem. 413, 6201–6212. [PubMed: 34468795]

Kucherenko IS, Sanborn D, Chen B, Garland N, Serhan M, Forzani E, Gomes C, Claussen JC, 2020. Ion-selective sensors based on laser-induced graphene for evaluating human hydration levels using urine samples. Advan. Mater. Tech. 5, 1901037.

Lai CZ, Fierke MA, Stein A, Bühlmann P, 2007. Ion-selective electrodes with three-dimensionally ordered macroporous carbon as the solid contact. Anal. Chem. 79, 4621–4626. [PubMed: 17508716]

Lazanas AC, Prodromidis MI, 2023. Electrochemical impedance spectroscopy– a tutorial. ACS Measurem. Sci. Au.

Lean I, DeGaris P, McNeil D, Block E, 2006. Hypocalcemia in dairy cows: meta-analysis and dietary cation anion difference theory revisited. J. Dairy Sci. 89, 669–684. [PubMed: 16428636]

Lee CW, Jeong SY, Kwon YW, Lee JU, Cho SC, Shin BS, 2022. Fabrication of laser-induced graphene-based multifunctional sensing platform for sweat ion and human motion monitoring. Sensor Actuator Phys. 334, 113320.

Li F, Ye J, Zhou M, Gan S, Zhang Q, Han D, Niu L, 2012. All-solid-state potassium-selective electrode using graphene as the solid contact. Analyst 137, 618–623. [PubMed: 22140676]

Lin J, Peng Z, Liu Y, Ruiz-Zepeda F, Ye R, Samuel EL, Yacaman MJ, Yakobson BI, Tour JM, 2014. Laser-induced porous graphene films from commercial polymers. Nat. Commun. 5, 5714. [PubMed: 25493446]

Lingenfelter P, Bartoszewicz B, Migdalski J, Sokalski T, Bućko MM, Filipek R, Lewenstam A, 2019. Reference electrodes with polymer-based membranes—comprehensive performance characteristics. Membranes 9, 161. [PubMed: 31795415]

Liu Y, Liu Y, Meng Z, Qin Y, Jiang D, Xi K, Wang P, 2020. Thiol-functionalized reduced graphene oxide as self-assembled ion-to-electron transducer for durable solid-contact ion-selective electrodes. Talanta 208, 120374. [PubMed: 31816715]

Lyu Y, Gan S, Bao Y, Zhong L, Xu J, Wang W, Liu Z, Ma Y, Yang G, Niu L, 2020. Solid-contact ion-selective electrodes: response mechanisms, transducer materials and wearable sensors. Membranes 10, 128. [PubMed: 32585903]

Mather RR, 2009. Surface modification of textiles by plasma treatments. In: Surface Modification of Textiles. Elsevier, pp. 296–317.

Matlock T, 2023. United states Department of Agriculture, National Agricultural Statistics Service. URL: https://www.nass.usda.gov/Newsroom/2023/01-31-2023.php.

Melie D, . Dairexnet webinar, “treatment and prevention of subclinical hypocalcemia, year = 2014, url = https://www.agproud.com/articles/23181-the-dos-and-don-ts-of-administering-calcium-to-hypocalcemic-cows,..

Morales-Narváez E, Baptista Pires LM, Zamora Gálvez A, Merkoçi A, 2017. Graphene-based Biosensors: Going Simple.

Mullen P, 1975. Clinical and biochemical responses to the treatment of milk fever. Vet. Rec. 97, 87–92. [PubMed: 1154631]

Novoselov KS, Geim AK, Morozov SV, Jiang D.e., Zhang Y, Dubonos SV, Grigorieva IV, Firsov AA, 2004. Electric field effect in atomically thin carbon films. Science 306, 666–669. [PubMed: 15499015]

Oetzel GR, 2012. An update on hypocalcemia on dairy farms. In: Proceedings of the Four-State Dairy Nutrition and Management Conference, pp. 80–85.

Omidi M, Fatehinya A, Farahani M, Akbari Z, Shahmoradi S, Yazdian F, Tahriri M, Moharamzadeh K, Tayebi L, Vashaee D, 2017. Characterization of biomaterials. In: Biomaterials for Oral and Dental Tissue Engineering. Elsevier, pp. 97–115.

Ong V, Soleimani A, Amirghasemi F, Khazaee Nejad S, Abdelmonem M, Razaviyayn M, Hosseinzadeh P, Comai L, Mousavi MP, 2023. Impedimetric sensing: an emerging tool for combating the covid-19 pandemic. Biosensors 13, 204. [PubMed: 36831970]

Pande C, Bhatnagar M, 1958. Formation of complex compounds between urea and alkaline earth halides. xi. the systems cax2 co (nh2) 2 h2o.(conductivity and viscosity). Z. Anorg. Allg. Chem. 295, 185–192.

Payne J, 1977. Parturient Paresis. Metabolic Diseases in Farm Animals. Heinemann Medical Books, London, UK, pp. 61–83.

Reinhardt TA, Lippolis JD, McCluskey BJ, Goff JP, Horst RL, 2011. Prevalence of subclinical hypocalcemia in dairy herds. Vet. J. 188, 122–124. [PubMed: 20434377]

Ren M, Zhang J, Tour JM, 2018. Laser-induced graphene synthesis of co3o4 in graphene for oxygen electrocatalysis and metal-air batteries. Carbon 139, 880–887.

Roche J, Berry D, 2006. Periparturient climatic, animal, and management factors influencing the incidence of milk fever in grazing systems. J. Dairy Sci. 89, 2775–2783. [PubMed: 16772597]

Soares RR, Hjort RG, Pola CC, Jing D, Cecon VS, Claussen JC, Gomes CL, 2023. Ion-selective electrodes based on laser-induced graphene as an alternative method for nitrite monitoring. Microchim. Acta 190, 43.

Soupir M, Smith E, Claussen J, Gomes C, Hartfiel L, Chen B, Van Belle B, McLamore E, Claussen JC, Gomes CL, 2022. Hydrophobic Laser-Induced Graphene Potentiometric Ion-Selective Electrodes for Nitrate Sensing.

Teekayupak K, Lomae A, Agir I, Chuaypen N, Dissayabutra T, Henry CS, Chailapakul O, Ozer T, Ruecha N, 2023. Large-scale fabrication of ion-selective electrodes for simultaneous detection of na+, k+, and ca2+ in biofluids using a smartphone-based potentiometric sensing platform. Microchim. Acta 190, 237.

Thilsing-Hansen T, Jørgensen R, Østergaard S, 2002. Milk fever control principles: a review. Acta Vet. Scand. 43, 1–19. [PubMed: 12071112]

Titus D, Samuel EJJ, Roopan SM, 2019. Nanoparticle characterization techniques. In: Green Synthesis, Characterization and Applications of Nanoparticles. Elsevier, pp. 303–319.

Veder JP, De Marco R, Patel K, Si P, Grygolowicz-Pawlak E, James M, Alam MT, Sohail M, Lee J, Pretsch E, et al. , 2013. Evidence for a surface confined ion-to-electron transduction reaction in solid-contact ion-selective electrodes based on poly (3-octylthiophene). Anal. Chem. 85, 10495–10502. [PubMed: 24080025]

Wan Z, Nguyen NT, Gao Y, Li Q, 2020. Laser induced graphene for biosensors. Sustain. Mater. Tech. 25, e00205.

Zhang H, He R, Niu Y, Han F, Li J, Zhang X, Xu F, 2022. Graphene-enabled wearable sensors for healthcare monitoring. Biosens. Bioelectron. 197, 113777. [PubMed: 34781177]

Zou XU, Cheong JH, Taitt BJ, Buhlmann P, 2013. Solid contact ion-selective electrodes with a well-controlled co (ii)/co (iii) redox buffer layer. Anal. Chem. 85, 9350–9355. [PubMed: 24047234]

Zou XU, Zhen XV, Cheong JH, Buhlmann P, 2014. Calibration-free ionophore-based ion-selective electrodes with a co (ii)/co (iii) redox couple-based solid contact. Anal. Chem. 86, 8687–8692. [PubMed: 25117517]

Cuartero M, Bishop J, Walker R, Acres RG, Bakker E, De Marco R, Crespo GA, 2016. Evidence of double layer/capacitive charging in carbon nanomaterial-based solid contact polymeric ion-selective electrodes. Chem. Commun. 52, 9703–9706.

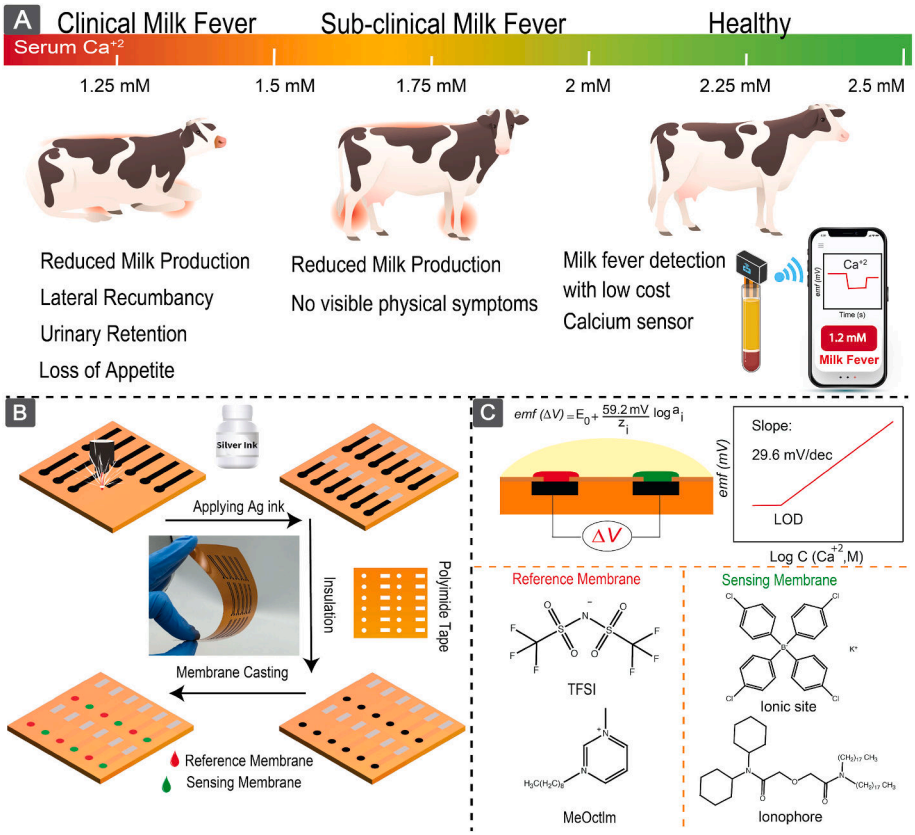

Fig. 1.

(A) Symptoms of clinical and subclinical milk fever. (B) Fabrication procedure of the sensor. (C) Membrane composition and working principle of the sensor.

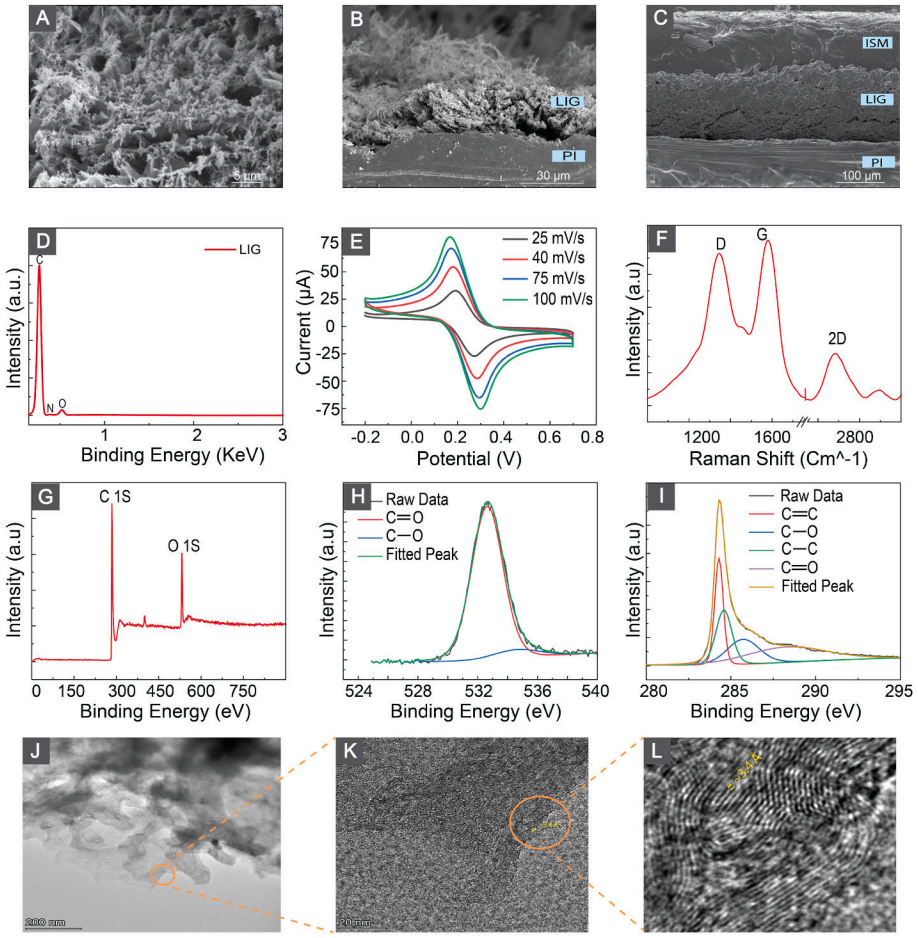

Fig. 2.

(A) Top-view SEM images of LIGs. (B) Cross-section SEM of LIGs. (C) Cross-section SEM of ISM on top of LIG. (D) EDX results and analysis of the LIG. (E) Cyclic voltammograms of the LIG electrodes at scan rates from 25 to 100 mV/s in 2 mM solution of $[Fe(CN)_6]^{3-/4-}$. (F) Raman spectrum of LIGs. (G) XPS survey on the surface of the LIGs. (H,I) XPS spectra for O 1s and C 1s respectively. (J) TEM image of LIG flakes. (K,L) High Resultion TEM (HRTEM) image of LIGs shows an average d-spacing of ≈ 3.4 Å that corresponds to the (002) planes of graphitic materials.

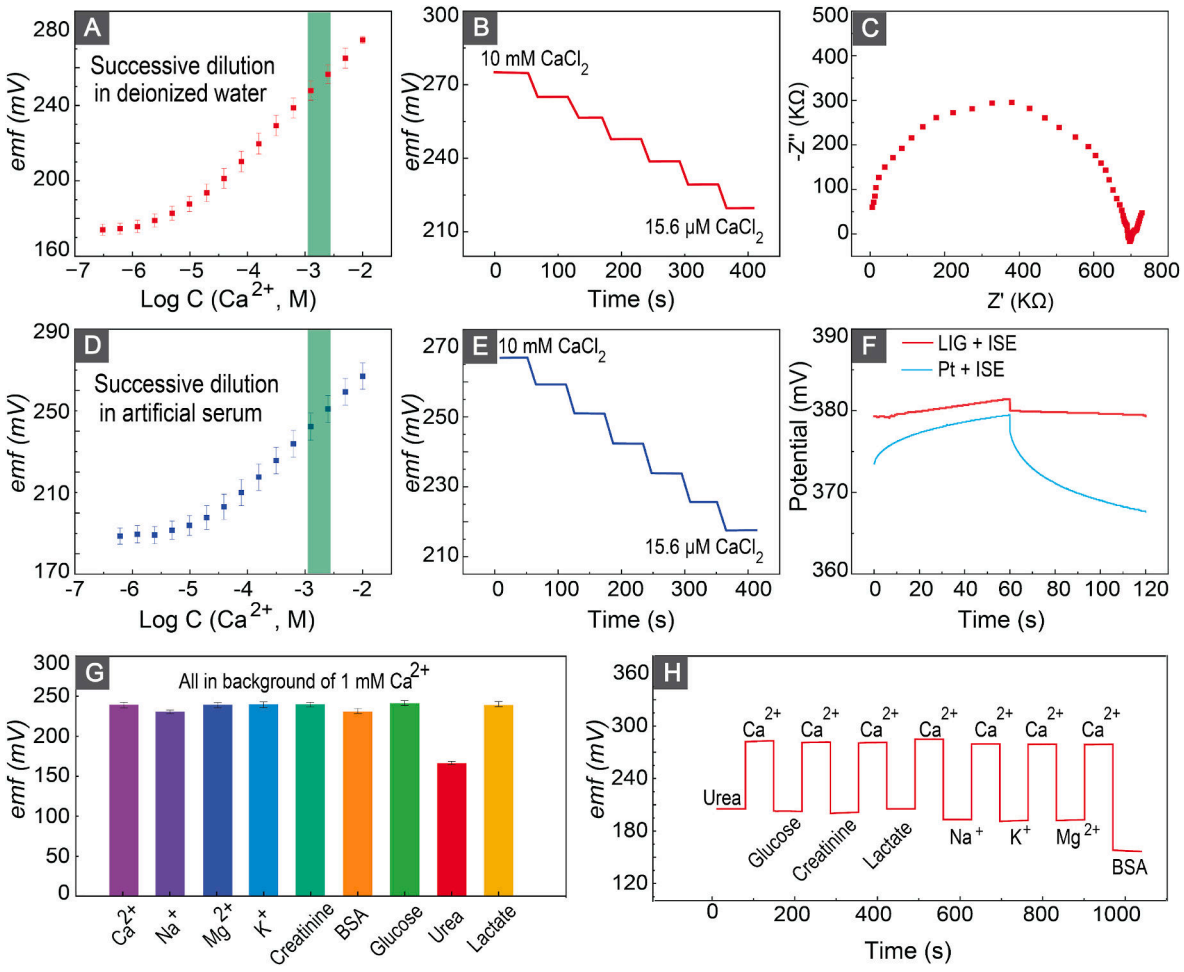

Fig. 3.

(A,D) Calibration curves of the calcium sensor in deionized water and artificial serum. Green shows the physiological relevant Ca^{2+} concentration in milk fever (B,E) Emf trace of the calcium sensor after successive half dilution process in deionized water and artificial serum. (C) EIS result of the sensor in 10 mM calcium chloride. (F) Chronopotentiometry results of a calcium membrane-coated Pt wire and calcium membrane-coated LIG to ± 1 nA perturbation current. (G) Response of a representative calcium sensor to different physiologically relevant ions and biologicals in the background of 1 mM $CaCl_2$. (H) Response and reversibility of the sensor after successive insertion of the sensor into $CaCl_2$ and different biologicals and ions.

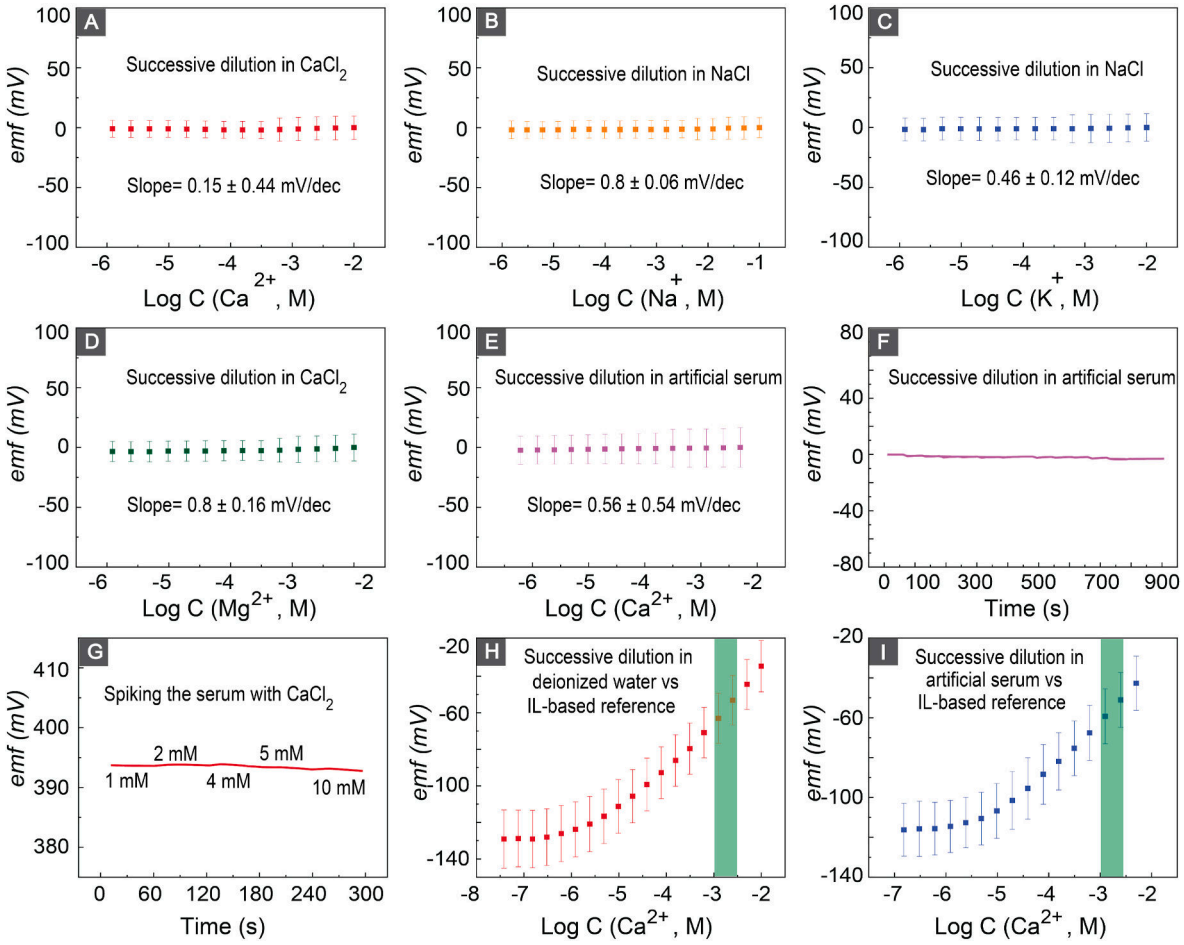

Fig. 4.

(A–D) Potential of the IL-based reference electrode in Ca^{2+}, Na^{+}, K^{+}, Mg^{2+}, solutions respectively. (E,F) Potential of the IL-based reference electrode after successive dilution of calcium in artificial serum.(G) Potential of IL-based reference electrodes after spiking the serum with Ca^{2+}. (H,I) Calibration curves of the calcium sensor versus IL-based reference electrode in deionized water and artificial serum respectively. Green bars highlight the physiological relevant Ca^{2+} concentration range in milk fever.

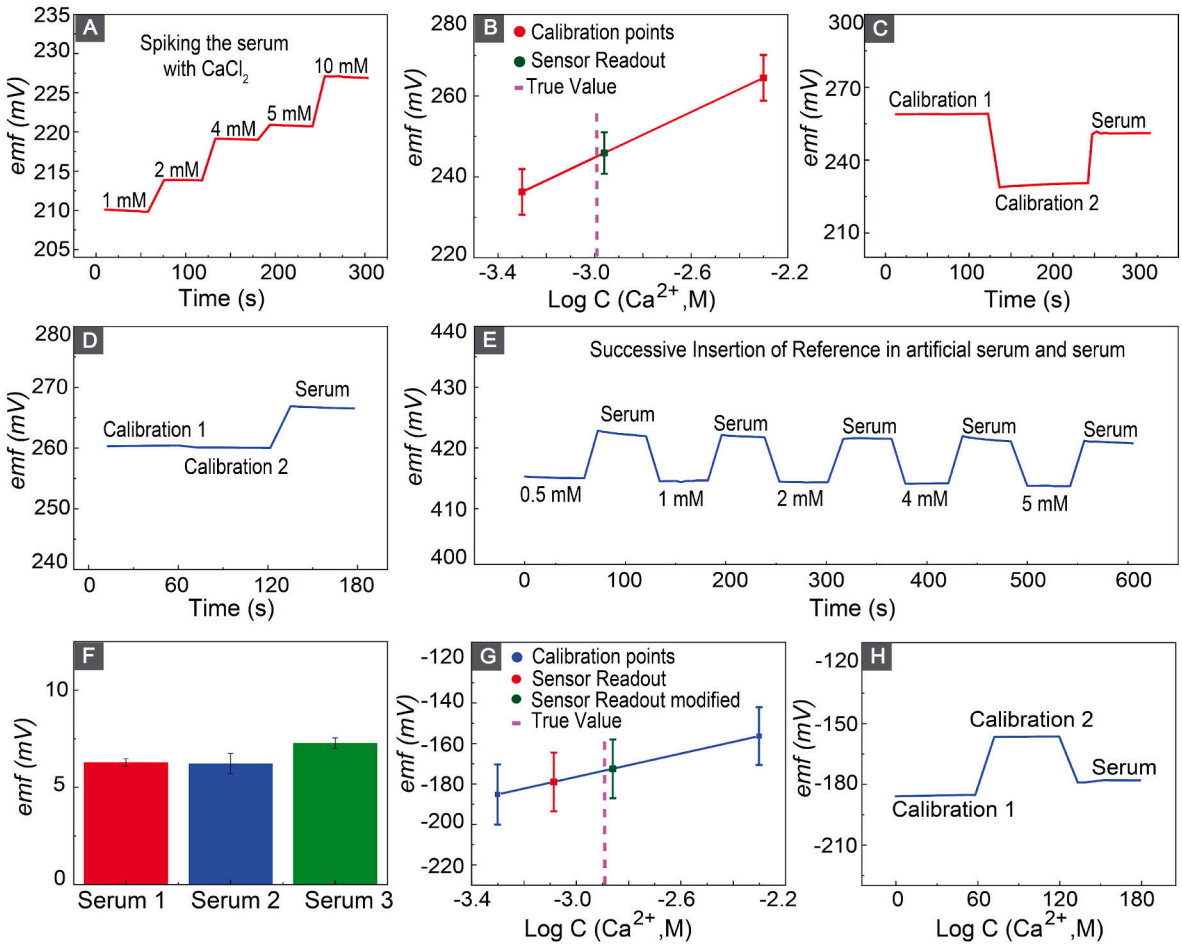

Fig. 5.

(A) Response of the calcium sensor after spiking the serum with Ca^{2+}. (B) Nernstian behavior of the sensor to two-point calibration in artificial serum and accuracy of the calcium sensor to measurement of calcium in serum. (C) Emf response of the calcium sensor to the insertion of the sensor in calibration solutions and serum. (D) Emf shift of the IL-based reference electrodes after electrode transfer from artificial serum to serum. (E) Similar shift in the emf response of the IL-based reference electrode after successive insertion of electrode in artificial serum with different Ca^{2+} concentration and serum. (F) Shift in the emf response of the Il-based reference electrode after transfer of the electrode from artificial serum to serum in three different adult bovine serums. (G) Nernstian behavior of the sensor in response to two-point calibration in artificial serum, as well as measured calcium levels before and after correcting for IL-based shift. (H) Emf response of the calcium sensor to the insertion of the sensor in calibration solutions and serum versus IL-based reference electrode.

Table 1

Ca^{2+} measurement in bovine serum and recovery using commercial and IL-based reference electrodes (n = 3). (Actual concentration of Ca^{2+} is measured by commercially available Horiba Ca^{2+} sensor).

Sensor	Actual Concentration (mM)	Measured Concentration (mM)	Error (%)
ISE vs. DJ-RE[a]	1.048	1.096	4.8
ISE vs. IL-RE[b]	1.250	1.366	9.3

[a]Double-Junction free flow Reference Electrode.

[b]Ionic Liquid Based Reference Electrode.